The facile conversion of waste biomass into few-layer graphene oxide

Final Report for Project number: 21-179

By: Oisik Das and Rhoda Afriyie Mensah (LTU)

Summary

A novel and sustainable method was employed to convert waste wood biomass directly into graphitic carbon without an amorphous intermediate, using manganese nitrate as a catalyst at varying concentrations (0.003 to 0.1 mol-metal/g) and treatment durations (1 and 2 hours). Doping the catalyst through vacuum soaking and mild heating (90°C) facilitated graphitic carbon formation at lower temperatures (<1000°C), eliminating the need for amorphous biochar production before graphitisation. After pyrolysis at 900°C and 950°C for 2 hours, the wood sample with 0.005 mol-metal/g catalyst heated at 950°C showed the highest graphitisation degree. This sample underwent further processing in a planetary ball mill with melamine as a dispersant for 30 minutes. Characterisation revealed a broad absorption peak at 230nm and semi-transparent sheets (3-8 layers), similar to graphene oxide. To assess applications, 2wt.% of the produced graphene oxide was added to polyamide 11 and wheat gluten plastics and subjected to a cone calorimeter, microscale combustion calorimeter (MCC), and mechanical tests. Results from the cone calorimeter demonstrated a 42% and 33% reduction in peak heat release rate compared to neat samples, showcasing the efficacy of few-layer graphene oxide as a fire-retardant additive for enhancing the fire safety of plastic materials. However, the MCC results revealed that the addition of GO had minimal effect on the combustion behavior of the plastics. On the other hand, the introduction of GO led to a notable decrease in the tensile strength of both materials. This suggests a trade-off between improved flame resistance and reduced mechanical strength. The intricate relationship between material composition and the dispersion of GO underscores the importance of a well-balanced approach when engineering advanced materials with tailored properties.

Keywords: Wood waste; Catalytic grahitisation; Graphitic carbons; Few-layer graphene oxide.

1. Introduction

In recent years, carbon-based materials have garnered significant attention due to their superior properties, including excellent chemical resistance, as well as thermal, mechanical, and electrical characteristics. These aforementioned properties have made them suitable candidates for various applications such as energy storage, nanocomposites, etc.[1–4] Amongst the different types of carbon structures, the most popular are graphene, carbon nanotubes, graphitic carbons, etc.[1,5–9] The ever-increasing need for these carbon-based materials has heightened the effect of their manufacturing on the environment.[10] The production of these carbon-based materials primarily relies on petroleum-based precursors, such as coke and coal. This constitutes one of the major drawbacks of the aforementioned materials because the base material is non-renewable and non-sustainable in nature.[11,12] Therefore, it is critical to adopt a novel approach where the starting material is bio-based while the process is non-hazardous involving fewer solvents, more catalytic reagents, and generating minimal waste products.[13] To decrease the dependence on petroleum products for developing carbon materials, biomass feedstock is being used as an alternative environment-friendly carbon source.[12,14,15] The advantages of biomass over petroleum-based counterparts are that it is renewable and economical as biomass can be converted to carbon at comparatively low temperatures.[16] Additionally, the pyrolysis process for biomass conversion into carbon is considered to be carbon-neutral owing to the carbon emission balancing ability of the feedstock.[12,17] Thus, high-value carbons (e.g. graphene oxide) can be engineered from renewable biomass, thereby propagating the concept of sustainable development.

Graphene oxide (GO) is a material that holds great potential in various fields due to its unique properties. It is derived from graphene, a two-dimensional carbon allotrope by introducing oxygen-containing functional groups such as hydroxyl (-OH), ethers (-O-), and carboxyl (-COOH) groups onto its surface.[18] These functional groups impart various structural and chemical modifications in graphene, which results in the

formation of GO. The presence of the functional groups gives GO its unique electronic and optical characteristics by creating defects and a bandgap in its structure, fostering the semiconductor nature of GO.[19] The oxygen groups on GO also provide sites for attaching other molecules, polymers, nanoparticles, etc. making it a versatile material for creating hybrid materials with tailored properties.[20] GO's large surface area, flexibility, and strength make it useful for energy storage, sensing, and environmental applications.[21] Most 2D carbon materials, including graphene and graphene oxide, are typically derived from graphite as a precursor. Graphite is a naturally occurring carbon material, but its extraction and processing can have environmental implications.[22] As the demand for graphene-based materials continues to grow, there is a need for greener and more sustainable methods of graphite production.

Graphitic carbon has attracted considerable attention over the last decade due to its potential applications in supercapacitors, composite manufacturing, solar energy, etc.[23,24] In spite of its diverse application potential, the main concerns associated with graphite production are the high-energy manufacturing methods (e.g. synthetic processes like the Acheson process, where silica is used at very high temperatures ca. 4150 °C).[16,25] The conventional route to obtaining high-quality graphite is by exposure to elevated temperatures (~3000 °C) or stress graphitisation of feedstocks that are rich in carbon.[26] However, the disadvantages of these methods include very high costs, challenges associated with scaling up the process, the severity of the processing conditions, etc.[9] The utilisation of metal catalysts like Fe, Mn, etc. for the graphitisation process can lower the treatment temperature to below 1000 °C.[27–31]

Numerous biomass feedstock has been used by various researchers for producing graphitic carbons with specific graphitic order.[32,33] However, one of the major challenges in converting biomass to graphitic carbon is the amorphous nature of the feedstock, which requires a catalyst to induce the formation of graphitic structure at temperatures below 1000 °C.[12,34–36] Literature shows that iron, cobalt, and manganese

are the best catalyst among different (like Ni, Mg, Ti, Cu, Cr, etc.) metals to produce graphitic carbon structures.[9,12,37,38] The mechanism behind this ordered structure formation in the presence of a metal catalyst is that the metal particle serves as a substrate for the carbon material to grow in an ordered manner.[9,39] Demir et al.[9] studied the catalytic graphitisation of lignin using a two-step process consisting of both hydrothermal carbonisation and simple pyrolysis at 900-1100 °C. Firstly, lignin is hydrothermally carbonised at 300 °C and 103 bar pressure to generate biochar, which then undergoes subsequent pyrolysis in the presence of three different catalysts (nitrate salt of Fe, Mn, and Co) at 900 – 1100 °C in N_2 atmosphere. A catalyst content of 0.083 mol-metal/g (for both Mn and Co catalyst) and temperatures of 900 and 1000 °C for $Mn(NO_3)_2$ and $Co(NO_3)_2$ respectively, were utilised. The results showed the obtained carbon was thermally stable and had good-quality graphitic carbon with both micro and mesoporous structures.

In another work, Major et al.[25] analysed the catalytic graphitisation of miscanthus grass using a hybrid catalyst with both Iron (III) and Cobalt (II) nitrates. They stated that the highest degree of graphitisation was attained due to the formation of Fe-Co alloy nanoparticles in the system. A 1:1 ratio of cobalt nitrate moles to iron nitrate moles was taken to make the total moles of metal in the system 0.00718 moles. The authors also stated that the yield of graphitic carbon in the pyrolysed sample can be increased by raising the pyrolysis temperature. The results obtained allowed for the use of such renewable graphitised biochar in applications like catalysis, electronics, and composites with enhanced sustainability and economic benefits compared to conventional graphitic carbons. Although a lot of research has been done on catalytic graphitisation of biomass feedstock, the final product properties depend greatly on the extent of graphitisation of the carbon material.

The present study represents an important step towards developing a more sustainable and efficient method for producing two-dimensional carbon structures. Graphitic

carbons were produced directly from biomass without an intermediate amorphous carbon step by impregnating the biomass with varying concentrations of manganese nitrate and pyrolysing at temperatures below 1000 °C. Low-energy intensive vacuum soaking and heating were adopted as efficient doping techniques to impregnate the catalyst into birch wood. The vacuum soaking step was not for the preparation of amorphous carbon, rather it was to dilate the pores of the wood for the catalyst to penetrate thereby stimulating the efficient formation of graphitic carbon during pyrolysis and at lower catalyst contents. The aforementioned process also avoids the use of organic solvents for the doping of the precursor material. Manganese nitrate was selected as the catalyst due to a prior study's findings, which indicated its superior degree of graphitisation in comparison to other metal catalysts.[9] The graphitic carbon produced was milled in the presence of melamine to produce few-layer graphene oxide. This approach has the potential to produce few-layer graphene oxide at a lower temperature than the traditional methods, making it more energy-efficient and cost-effective. It also provides a means of producing bulk graphene, which can be used in a variety of applications, such as in the production of composites, batteries, and electronic devices. To explore the applications, the few-layer graphene oxide produced in this project was incorporated into wheat gluten and polyamide 11 plastics to investigate the effect on their fire performance using reaction-to-fire properties from cone calorimeter tests.

2. Experimental

2.1. Materials:

The biomass feedstock used for the catalytic graphitisation in this study was hardwood (birch), which is a widely available natural resource in Sweden that also gets naturally regenerated. Milled birch wood waste was sieved to a size of ca. 100 – 200 microns. The catalyst, Manganese (II) nitrate hydrate (98%) [$Mn(NO_3)_2$] (CAS No.: 15710-66-4), and melamine (CAS No.: 108-78-1) were purchased from Sigma Aldrich. Distilled water (DI) was used for all the wet procedures in the present work.

The wheat gluten (WG) matrix for the composites was obtained from Lantmännen Reppe AB in Sweden and had a gluten protein content of 86.3 ± 0.3%, along with 0.9 ± 0.1% fat and 0.8 ± 0.1% ash. The powder form of Polyamide 11 (PA 11) was procured from Arkema in France.

2.2. Doping of catalyst into wood:

To increase the effectiveness of the catalyst in the graphitisation process, the catalyst, $Mn(NO_3)_2$, was first dissolved in DI water as a 10 % solution before wood impregnation. For the doping process, 30 g of the wood particles were placed in a 10 % solution of $Mn(NO_3)_2$ having concentrations of 0.003, 0.005, 0.083, and 0.1 mol-metal/g. The wood particles were soaked under vacuum for 12 h. The vacuum soaking aided in pushing out pockets of air from the pores of the wood particles for easy penetration of the catalyst. These four catalyst concentrations were chosen for the study based on previous reports, where these are one of the lowest and highest amounts of catalyst used for graphitisation.[9] The wood particles for each concentration were filtered and doping was done by just heating between 80 – 90 °C for one and two h without the application of any pressure. The doped wood particles were kept in an air oven at 60 °C for 48 h to remove the moisture.

2.3. Pyrolysis of catalyst-doped wood (Graphite production):

The moisture-free doped wood particles were initially pyrolysed at 900 °C in an inert atmosphere for two h in a macro thermogravimetric analyser (macro-TG reactor) using a nitrogen flow rate of 10 l/h. [40] The catalyst-doped wood particles after pyrolysis were washed with dilute HCl, a few times, to remove the excess metal constituents (MgO salts) from the final product. The different samples prepared, along with their code names and processing conditions are shown in Table 1.

Table 1: Description of different pyrolysed samples and their coding.

Sample Name	Amount of catalyst (mol-metal/g)/Description
1C	0.003/1 h heating time
1D	0.003/2 h heating time
2C	0.005/1 h heating time
2D	0.005/2 h heating time
3C	0.083/1 h heating time
3D	0.083/2 h heating time
4C	0.1/1 h heating time
4D	0.1/2 h heating time

After characterisation and analysis, the pyrolysis process was repeated for the samples with low catalyst content (1C, 1D, 2C, and 2D). For this step, the pyrolysis temperature was increased to 950 °C to increase the yield of graphite.

2.4. Processing graphite to few-layer graphene oxide:

The graphitic carbon from the selected sample 2D (0.005 mol-metal/g of $Mn(NO_3)_2$ heated for 2 h) was mixed with melamine at a ratio of 1:3, one part graphite, and 3 parts melamine according to the work of León et al.[41] The graphite-melamine mixture was milled i.e., mechanically exfoliated in a planetary ball mill set at 100 rpm for 30 mins. The milled graphite-melamine mixture was washed with distilled water heated at 60 °C to remove all traces of melamine, filtered, and dried at 100 °C for 30 mins.

2.5. Composite manufacturing:

WG and PA11 were mixed directly with 2wt.% graphene oxide (GO) in a vortex mixer and 3g of each mixture was moulded using Fortijne Presses TP 400 from the Netherlands. For samples based on wheat gluten (WG), the compression was performed at a temperature of 150 °C, a force of 290 kN, and a pressing time of 30 minutes. In the

case of samples based on PA 11, the compression was carried out at a temperature of 200 °C, a force of 250 kN, and a pressing time of 30 minutes.

2.6. Characterisation of graphitic carbons

2.6.1. Scanning electron microscopy (SEM):

The samples were analysed in an FEI Magellan 400 field emission XHR-SEM instrument at an accelerated voltage of 3 kV and a current of 6.3 A.

2.6.2. X-ray diffractometry (XRD):

The XRD diffractograms of the powder samples were recorded by placing the sample in the holder and then recording the diffraction patterns using Cu kα radiation. The equipment (PANalytical EMPYREAN) is fitted with a PixCel3D detector and a graphite monochromator. The diffraction was measured by scanning 2θ from 0 to 120 °. The anti-divergence slit and anti-scatter slit were fixed at 1/8 and ¼, respectively, during the analysis. The instrument was operated at 45kV voltage and 40 mA current.

2.6.3. Raman Spectroscopy:

The relative amounts of graphitic carbon and disorder associated with the samples were analysed using Raman spectroscopy. Raman spectra of the powder samples were measured using a home-built Raman set-up, which was detailed in our previous work.[42] The samples were excited at a wavelength of 532 nm, with a power density of 6×10^3 mW/mm^2. Each spectrum is an average of four spectra with a total acquisition time of 400 seconds. Each sample was measured several times in an air and nitrogen environment to ensure there was no oxidation that could bias the results.

2.6.4. Nanoindentation studies:

The hardness and reduced modulus of the samples were determined using a nanoindenter (Hysitron TI-950 triboindenter having a three-sided diamond Berkovich tip). The samples were mounted in epoxy set resin and then ground and polished after

12 h of curing. A standard quasi-static load function was used for a total of 12 indents where the maximum load applied was 10 μN on relatively flat sample surfaces found using an optical microscope with a 20 × objective magnification. Hardness and reduced modulus were calculated from the load–displacement data as specified in an earlier study.[43]

2.7. Characterisation of graphene oxide

2.7.1. Ultraviolet–Visible Spectroscopy (UV-Vis):

The absorbance of the graphene oxide sample was measured with UV-Vis. A Hitachi UV-Vis U-1500 spectrophotometer was used for the experiment. The sample was dispersed in water and analysed in a 1 cm wide cuvette at a range of 200 nm to 400 nm.

2.7.2. Transmission Electron Microscopy (TEM):

The morphology of the milled sample was observed in a 300 kV Hitachi HF-3300S TEM equipped with a cold field emission emitter and energy-dispersive X-ray spectroscopy (EDX). The micrographs were taken at an accelerating voltage of 100 kV.

2.8. Characterisation of composite samples (Cone Calorimeter tests):

The reaction-to-fire characteristics, peak heat release rate (PHRR), time to ignition (TTI), and total heat release (THR), of the specimens were assessed using a TCC 918 cone calorimeter from Netzsch Analyzing & Testing. The samples were exposed to a heat flux of 25 kW/m² until the flame extinguished. The ISO 5660–1:2015 standard was employed for conducting the test.

2.9. Microscale combustion calorimeter (MCC):

The heat release properties of the neat and GO-filled samples were measured using an FAA Micro Calorimeter from Fire Testing Technology (FTT), United Kingdom. Samples with sizes ranging from 8 – 10 mg were tested using the thermal decomposition method (Method A). The samples were pyrolysed in nitrogen from 150

– 750 °C and the effluent was combusted in oxygen at 900 °C with flow rates of 80 and 20 cc/min, respectively.

2.10. Tensile tests:

A criterion model 43 universal testing machine (MTS Systems Corporation, Créteil, France) was utilized for the tensile test using 3 replicates. The 500N load cell (model: LPB.502 D) was used for the wheat gluten/GO samples; while 50 kN load cell (model: LPB.504 C) was used for the polyamide 66/GO samples. The use of different load cell was due to the different strengths of the testing polymeric materials. The pulling speed was set at 0.1 mm/s. The tensile strength was calculated by the following equation:

$$f_{t,o} = \frac{F_{max}}{A}$$

Where $f_{t,o}$ is the tensile strength, F_{max} is the maximum load, and A is the area.

2.11. Hardness tests:

A depth-controlled surface hardness test was carried out according to the JIS Z 2101 standard, where the indenter was pressed into the specimen at a constant speed of 0.5 mm/min until the target depth of 0.32 mm was reached.

3. Results and discussion

3.1. Characterisation of graphitic carbons

3.1.1. Scanning Electron Microscopy (Morphology):

Figure 1 portrays the representative SEM micrographs of the pyrolysed catalyst-doped wood. It can be observed that the doping of the catalyst has promoted the formation of three-dimensional graphite, especially visible in samples with a lower amount of catalyst (Fig.1: 1C, 1D, 2C, and 2D). The carbon structure in these samples has a flaked nature, which is also arranged in layers, analogous to a graphite structure. The doped samples with a higher amount of catalyst (3C, 3D, 4C, 4D) also exhibit graphitic structure, however, these samples have a significant amount of metal oxide (MnO) coating the carbon surface. Hence, the samples containing a higher amount of catalyst

display a metal-carbon mixed structure as also shown by Demir et al.[9] From the SEM analysis, it can be stated that a low amount of catalyst (i.e., 0.003 and 0.005 mol metal/g) was apt for the generation of graphitic carbon without the presence of extra metal oxides remaining on the carbon surface. The high amount of catalyst (i.e., 0.083 and 0.1 mol metal/g), although can generate graphitic carbon, leaves behind some metal oxide deposits that consequently reduce the quality of the graphitic carbon.

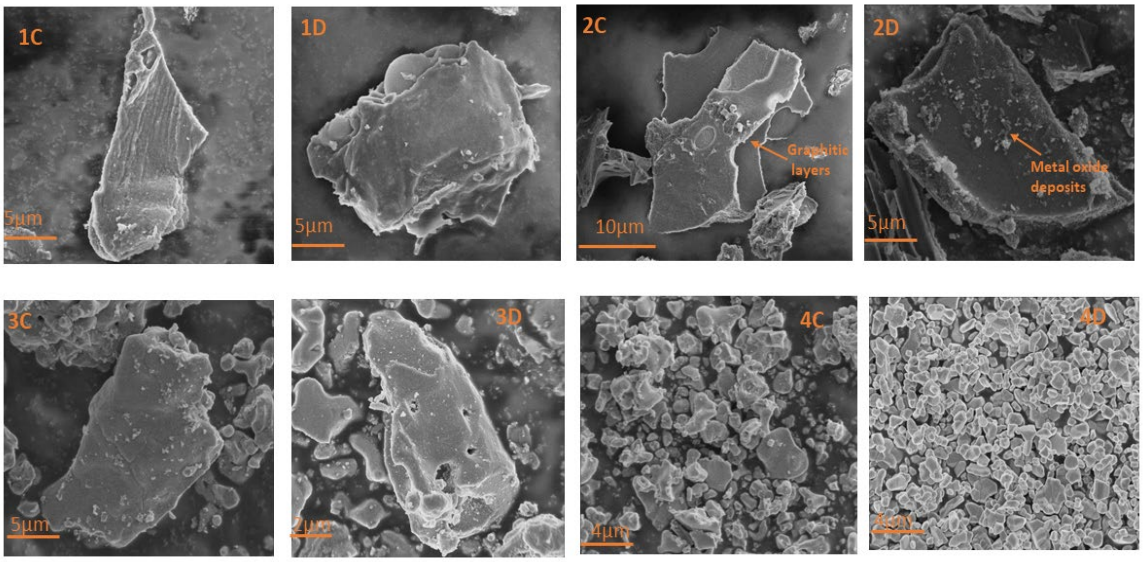

Fig. 1: SEM images of pyrolysed samples

3.1.2. X-ray diffractometry:

Further confirmation and information on the graphitisation process and the extent of graphitisation can be achieved via XRD analysis. The XRD diffractograms of catalyst-doped wood pyrolysed at 900 °C are shown in Figures 2a and 2b. It is observed that no characteristic peak of graphite (002 peaks at $2\theta = 26^{o}$) can be seen in the XRD pattern. The samples with low catalyst concentrations (1C, 1D, and 2C) showed a very amorphous structure, which does not corroborate the SEM results (Figure 1). The possible explanation for this observation is that the yield of graphite in the samples was very low, hence, only the amorphous particles were captured in the XRD. Only a broad hump can be seen in all the samples in Figure 2a signifying the presence of large quantities of amorphous carbon compared to the crystalline equivalent (Figure 2b). The reason could also be due to inefficient dispersion of the catalyst within the material leading to low-quality graphitic carbon. As already mentioned, catalytic graphitisation

is predominantly efficient when a higher amount of amorphous carbon comes in contact with the metallic entity during the graphitisation process. Thus, during graphitisation, carbon comes in contact with the metallic part leading to good-quality graphitic carbon as the end product.

However, it should also be noted that with increasing catalyst content, the removal of the same becomes difficult and the peaks due to these metallic constituents can be noticeably seen in the XRD. The presence of these metallic impurities in the sample after washing interferes with the XRD analysis. Interestingly, the samples with high catalyst content (2D, 3C, 3D, 4C, and 4D) shown in Fig. 2b displayed several characteristic peaks showing a crystalline structure. However, the peak with the highest intensity shifted from 26° for graphitic carbons to 32°. These revealed that although the samples had a high crystallinity, the structures were different from that of graphitic carbons. This could be attributed to the presence of MnO salts coating the surface of the samples. The 002 peak Scherrer equation (equation 1) was adopted to define the crystallite size of the graphite sheets in the crystalline samples along with the d-spacing values, which are shown in Table 2.

$$L_c = \frac{k\lambda}{\beta \cos\theta} \quad (1)$$

Where, k is a dimensionless shape factor with its value close to unity, λ is the wavelength of the X-Ray used, β is the line broadening at half the maximum intensity (FWHM) and θ is the Bragg angle. To determine the d-spacing values, Braggs law was used (equation 2).

$$2d \sin\theta = n\lambda \quad (2)$$

Where, d is the interplanar spacing, θ is the angle between the lattice planes and the wave vector of the incident wave, λ is the wavelength and n is the order of the reflection.

The graphitisation degree parameter (g) was then calculated using the following equation:

$$g = \frac{0.344 - d_{002}}{0.0086} \quad (3)$$

Previous research has shown that graphitic carbons have a d-spacing ranging from 0.335 – 0.34 Å.[37] According to Table 2, the d-spacing calculated for all the crystalline samples was less than 0.335, which shows that the samples contain large quantities of salts. To increase the yield of graphite, the experiments were repeated for the samples with low catalyst content (1C, 1D, 2C, and 2D), and the pyrolysis temperature was increased to 950 ^{o}C. The X-ray diffractograms of the samples were obtained and the parameters were estimated using Equations 1-3. The results are presented in Figure 2c and Table 3.

The curves in Figure 2c show a 002 peak between 25.6^{o} – 26.3^{o} and a 101 peak at 43^{o} giving d spacing values ranging from 3.47 – 3.38 Å. According to Vlahov[44], the d spacing of graphitic carbons is classified as fully ordered graphite (3.354 Å) to completely disordered graphite (3.440 Å). From Table 3, it can be inferred that samples 1C and 1D (with catalyst content of 0.003 mol metal/g) fall out of the range of graphitic carbons and have disordered graphite, however, 2C and 2D exhibit ordered graphitic structure with a graphitisation degree of ca. 58% and 70%, respectively. It can also be seen that the samples showed no traces of MnO salts.

Table 2: XRD data, d-spacing, graphitisation degree parameter, and crystallite size of catalyst-doped samples pyrolysed at 900 ºC.

Sample name	2 Theta (degree)	d-spacing (Å)	Graphitisation degree	Full Width Half Max.	Crystallite size (nm)
4D	28.8	0.309	0.398	0.20675	6.923887
4C	28.67	0.311	0.382	34.6696	0.041278
3D	29.11	0.307	0.436	-	-
3C	29.08	0.306	0.432	0.26766	5.351627
2D	29.19	0.305	0.445	0.26811	5.343978

Table 3: XRD data, d-spacing, graphitisation degree parameter, and crystallite size of low catalyst samples pyrolysed at 950 ºC.

Sample name	2 Theta (degree)	d spacing (Å)	Graphitisation degree (%)	FWHM	Crystallite size (nm)
1C	25.66	3.47	-	0.92	100
1D	25.59	3.45	-	1.12	62
2C	26.20	3.39	58.12	0.75	96
2D	26.33	3.38	69.77	1.12	62

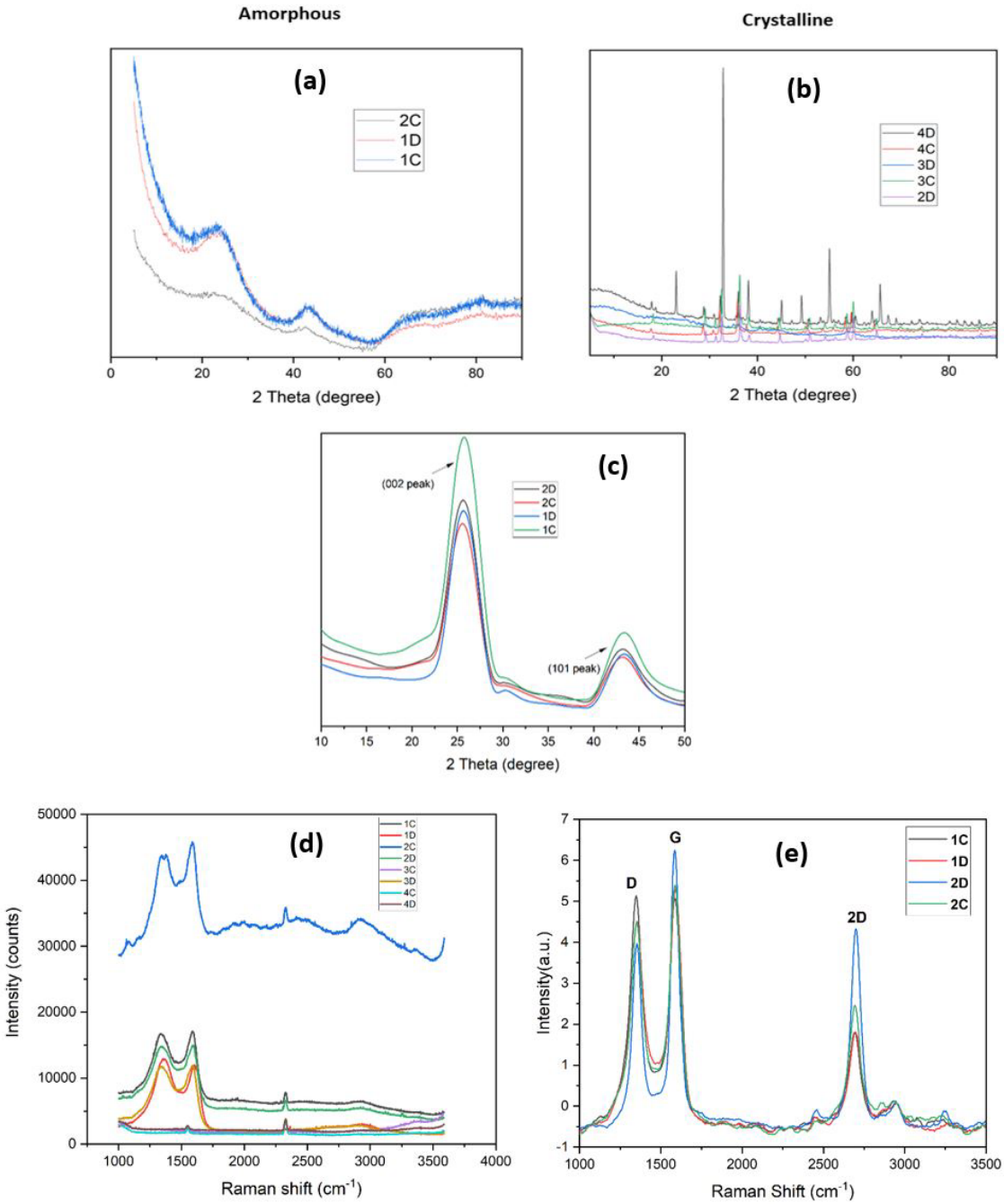

Fig. 2: XRD and Raman spectrometry characterisation of carbon samples; (a) and (b) XRD results of catalyst-doped wood pyrolysed at 900 °C; (c) XRD results of catalyst-doped wood pyrolysed at 950 °C; Raman spectra of catalyst-doped wood pyrolysed at (d) 900 °C and (e) 950 °C.

3.1.3. Raman Spectroscopy:

Generally, the Raman spectra of high graphitic materials such as graphite or multilayer graphene show three distinct peaks, namely the G band, D band, and 2D band due to in-plane vibrations. The G band, seen around ~1580 cm^{-1}, is associated with the in-plane bond-stretching vibrations of sp^2-bonded carbon atoms. In a two-dimensional hexagonal lattice, it is a measure of the degree of graphitisation of the materials.[45,46] The D band at ~ 1350 cm^{-1} is associated with the breathing mode of aromatic rings, which is activated by the presence of defects and edges in the materials. This peak area depends on concentration and types of defects.[47] The 2D band (~ 2700 cm^{-1}), on the other hand, is the D-peak overtone which does not require the defect presence. For few-layer graphene, this band is sensitive to the number of graphene layers present in the material.[48]

The results from the Raman experiments of samples pyrolysed at 900 °C are plotted in Figure 2d. Most of the samples show D and G peaks in their spectra indicating the presence of the graphitic structure, while 3C and 4C show no graphitic structure. The widths of D and G are rather large (~ 100 cm^{-1}) and their second-order peaks (from 2400 cm^{-1} to 3600 cm^{-1}) are very weak. The 2D peak cannot be observed. These features indicate disordered structures. There is a peak at ca. 2300 cm^{-1}, which is a result of the nitrogen in the air.[49] Sample 2C had the highest intensity counts, which is also supported by the distinct graphitic layers in the SEM images in Figure 1.

The Raman spectra of the four selected samples with low catalyst concentration (1C, 1D, 2C, and 2D) pyrolysed at 950 °C are shown in Figure 2e. The figure shows separated D and G bands with narrower bandwidths (a few tens of cm^{-1}) along with very distinct 2D peaks signifying the presence of graphitic carbons. Table 4 presents the peak positions and analysis made from the Raman spectra.

Table 4: Positions of D, G, and 2D bands and analysis from the Raman spectra.

Sample	Position of D band (cm^{-1})	Position of G band (cm^{-1})	Position of 2D band (cm^{-1})	I_D/I_G	Number of graphitic layers
1C	1353	1585	2691	1.0	1.7
1D	1350	1584	2691	0.84	2.8
2C	1354	1583	2695	0.82	3.9
2D	1354	1584	2701	0.62	3.0

The number of graphitic layers was calculated using Equation (4).

$$w_G = 1581.6 + \frac{11}{1 + n^{1.6}} \quad (4)$$

Where w_G is the G band position in wavenumbers, and n is the number of layers present in the sample.[50] The I_D/I_G ratio obtained from the Raman spectra can be used as an effective tool to distinguish the extent of graphitisation and defects in a material, in particular, the size of the basic graphitic structural unit is inversely proportional to I_D/I_G.[51] The lower the I_D/I_G ratio, the lesser will be the defects or disorders associated with the system and depicts a higher amount of crystalline or graphitic content in the final product.[52]

It can be seen in Table 4 that the intensity ratio, I_D/I_G, decreases with increasing catalyst concentration and heating time. Sample 2D had the lowest intensity ratio depicting lower defects in the graphitic structure, corroborated by the highest intensity 2D peak in Figure 2e. The estimation of the number of graphitic layers showed that all the samples displayed more than one layer of graphene.

From the Raman and XRD results, sample 2D (0.005 mol-metal/g of $Mn(NO_3)_2$) displayed the best graphitisation degree and lowest defects in the graphitic structure, hence, this sample was chosen for further analysis.

3.1.4. Nanoindentation

Nanoindentation tests were performed on the 2D graphite sample to measure its mechanical properties, hardness, and modulus. A Berkovich indenter applied a controlled force to the graphite, creating a small indentation on its surface. By measuring the force and displacement of the indenter, the mechanical properties were calculated.[53] Graphite is a layered material consisting of stacked sheets of hexagonally arranged carbon atoms. Within each sheet, the carbon atoms are covalently bonded, however, there are weak Van der Waals forces between adjacent sheets, which allow them to slide past one another. This weak interlayer bonding makes graphite relatively soft and deformable in the direction perpendicular to the sheets, while being very stiff and strong in the plane of the sheets.[54] The results obtained from the nanoindentation tests are as follows; Hardness: 0.225 ± 0.025 GPa and calculated elastic modulus: 0.22 ± 0.017 GPa. Figure 3a shows the load versus displacement curve of the 2D graphite sample compared to the nanoindentation results of biochar shown in the work of Das et al[55], where the hardness of biochar was reported to be 5 GPa and an elastic modulus of ca. 0.5 GPa. It is seen that the hardness and elastic modulus of the graphite from sample 2D was approximately 96% and 56% lower than that of biochar, respectively.[56] This signifies that biochar has high resistance to indentation and plastic deformation compared to graphite. The catalyst impregnation and higher treatment temperature aided an increase in the degree of graphitisation of the biomass. The layers of the graphitic sheets allowed slipping of the basal planes during indentation, leading to a reduction in the hardness values. The orientation of the graphitic sheets caused the moduli to decrease in this sample. Therefore, it can be inferred that the nanoindentation hardness and modulus decrease with the increasing degree of graphitisation of carbon materials.

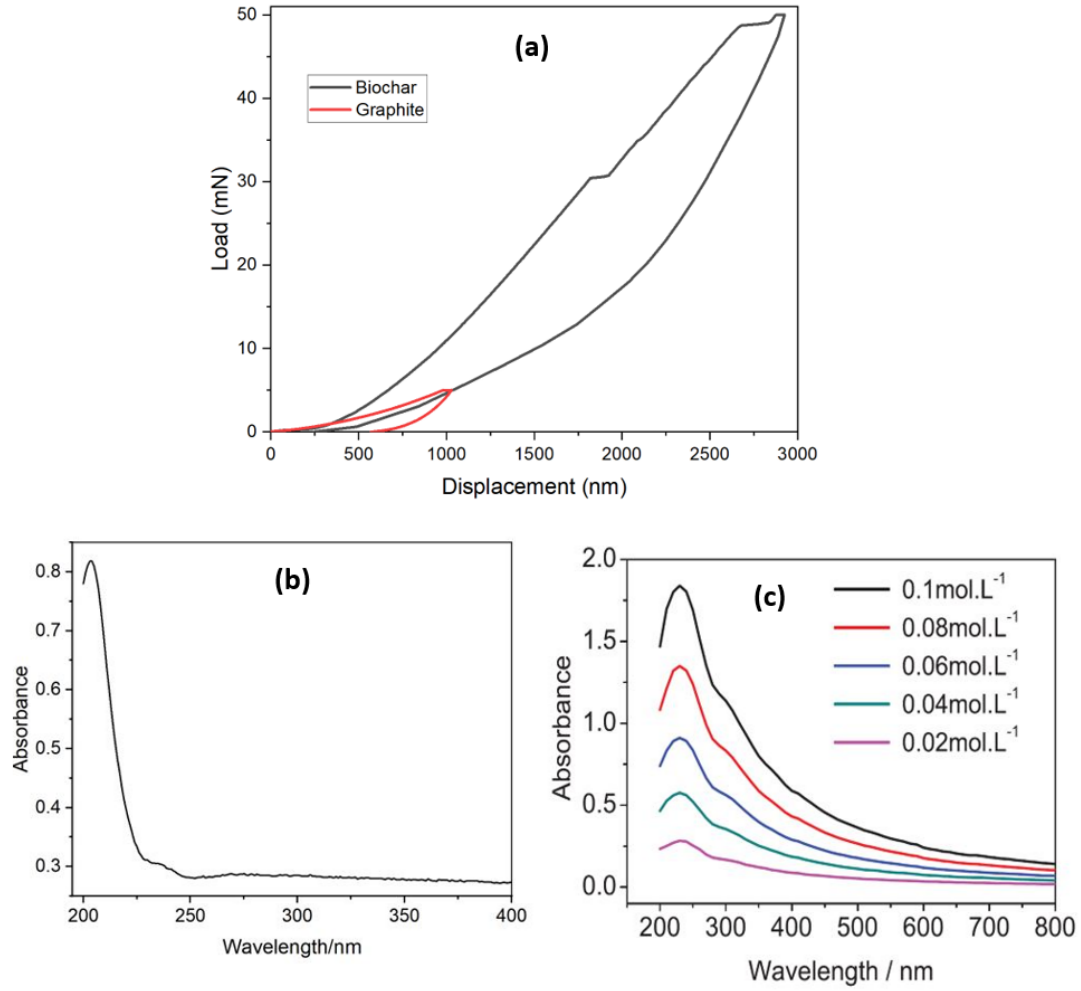

Fig. 3: (a) Nanoindentation results (load versus displacement curves for 2D graphite sample compared with biochar from Das et al[55]; (b) UV-Vis results for sample 2D compared with (c) UV-Vis results of graphene dispersions by Lai et al[57]

3.2. Production of Graphene oxide

Few-layer graphene oxide was produced by adopting the mechanical exfoliation method. In this method, the graphite with the highest graphitisation degree (2D) together with melamine was milled in a planetary ball mill to separate the layers using mechanical force. The melamine acted as a dispersant that aids the graphene flakes from re-aggregating. Additionally, the melamine reduced the surface tension between the graphite flakes making it easier to separate.

During the milling process, the melamine molecules are inserted between the layers of graphite in a process called intercalation. This leads to the expansion of the graphite layers resulting in easier separation into individual graphene layers. The as-produced few-layer graphene oxide was analysed using Ultraviolet-Visible Spectroscopy, Energy Dispersive X-Ray Spectroscopy, and Transmission Electron Microscopy methods.

3.2.1. Ultraviolet–Visible Spectroscopy

The UV-Vis technique measures the absorbance of light at different wavelengths by a sample, which can provide information on its electronic and optical properties. Graphene dispersions typically show an absorbance peak around 210-300 nm due to π-π * transitions of the sp^2 domains.[58] The result from the UV-Vis test of the milled 2D sample is shown in Figure 3b. The fluorescence pattern found between the wavelengths of 200 to 250 nm is similar to the results for graphene oxide dispersions found in other studies, also shown in Figure 3c.[57] Figure 3b shows a peak at ca. 230 nm, which is a result of aromatic C-C bonds in graphene oxide.[59] It was, however, noticed that the absorption peak is not very sharp but rather spread out. This broadening shows the presence of different electronic transitions happening within the material due to graphene oxide having a somewhat disordered structure and the different oxygen functional groups attached to it. These factors create variations in the energy levels of the electronic states, resulting in a broader range of absorption wavelengths. Additionally, the introduction of oxygen functional groups and defects disrupts the π-conjugation within the graphene lattice, resulting in a decrease in the bandgap and a shift towards longer wavelengths.[58,60] Based on the comparison from literature, it can be inferred that the graphite was successfully converted to graphene oxide. Further investigations were carried out with Energy-dispersive X-ray spectroscopy (EDX) and TEM.

3.2.2. Energy Dispersive X-Ray Spectroscopy (EDX)

EDX analyses the elemental composition of samples by providing information on the types of elements present in a sample and their relative abundance. This technique was used to characterise the milled 2D sample to determine its composition. Figure 4a shows the EDX map of the sample whereas the elemental constituents with their corresponding weight percentages are listed in Table 5. The results show that the sample contains ca. 91 % carbon, 5 % nitrogen, and 4 % oxygen. The EDX results clearly reveal the presence of oxygen in the sample, indicating that the graphene was oxidised during milling/processing as confirmed in the work of Mahmoud et al[61] where the ball milling time for processing graphite into graphene affected the degree of oxidation of the end product. The nitrogen element identified could be attributed to the presence of nitrogen-containing functional groups or impurities during the synthesis or oxidation process. It should be noted that the presence of nitrogen in graphene oxide can enhance its properties and introduce additional functionality such as increasing the charge carrier density and facilitating better electrical conductivity. Nitrogen atoms can also serve as active sites for redox reactions, improving the charge storage capacity and overall performance of supercapacitors and lithium-ion batteries.[62]

Table 5: Elemental composition of sample 2D from EDX

Element	Wt%	Absorption correction
C	90.45 ± 1.8	1.2
N	5.20 ± 1.3	4.6
O	4.34 ± 0.55	2.7

3.2.3. Transmission Electron Microscopy (TEM)

The morphology and internal structure of the milled 2D sample were observed using TEM. In the TEM, graphene oxide sheets have distinctive characteristics. They show irregular shapes (edges) and sizes with variable thicknesses due to the oxidation

process.[63] The micrographs of the milled 2D samples are illustrated in Figures 4b and 4c. Figure 4b shows the irregular and stacked layers of the graphene oxide, which was achieved as a result of the impact forces generated from the collisions of the balls in the planetary ball mill that allowed for the sliding of the graphite particles. Some wrinkles and folds as well as the variation in layers (from 3 to 8 layers) are present in the structure, which are caused by the introduction of oxygen functional groups. An estimation of the spacing between the layers in Figure 4b revealed a distance of ca. 0.34 nm. Some regions of the sample were more compact due to aggregation of the particles. Figure 4c shows a semi-transparent structure akin to graphene oxide micrographs reported by Aziz et al.[64]

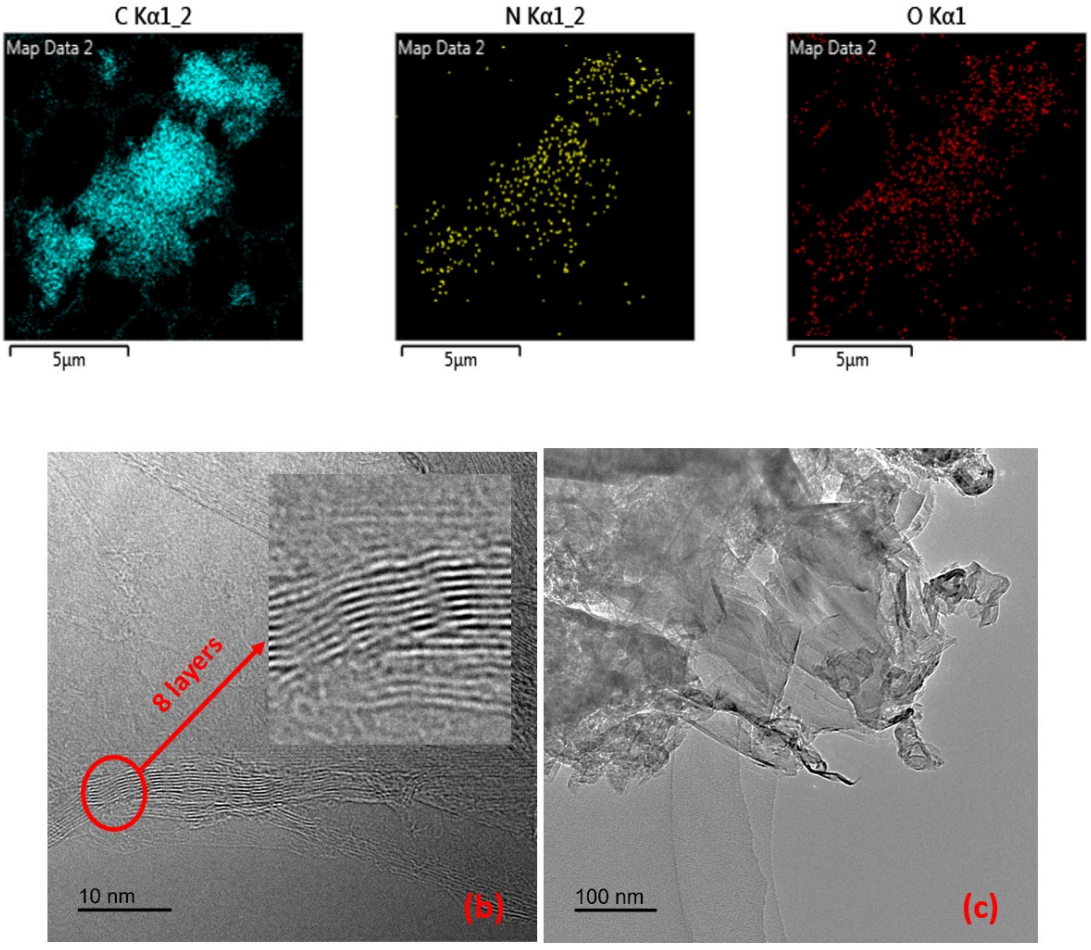

Fig. 4: (a) EDX map of milled 2D sample; TEM micrographs of the milled 2D sample showing (b) the stacked layers, wrinkles, and folds (c) the semi-transparent nature similar to that of graphene oxide.

Following the results from UV-Vis, EDX, and TEM, it is evident that few-layer graphene oxide has been successfully produced from waste birch wood.

3.3. Composite Manufacturing

The GO was incorporated in biobased plastic (WG) and synthetic plastic (PA11) to ascertain the effect on their reaction-to-fire from cone calorimeter tests and heat release properties from MCC tests. The mechanical properties were also obtained by conducting tensile and hardness tests.

3.3.1. Cone Calorimeter Results

The heat release curves measured from the cone calorimeter are depicted in Figure 5, while the reaction-to-fire properties of the samples are presented in Table 6. It is seen that the addition of 2 wt.% GO significantly reduced the peak heat release rate of the samples, with a reduction of 42% in neat PA11 and 33% in neat WG. The two-dimensional structure of GO forms a surface barrier that prevents the release of volatile substances and flammable gases. Additionally, the high thermal conductivity of GO improves heat dissipation, limiting combustion propagation. It was also clearly seen during the experiment that the functional groups in GO serve as catalysts during thermal degradation, assisting in the creation of a char layer that protects and lowers flammability.[65]

The time to ignition (TTI) of neat PA11 decreased by 51% with the addition of GO, while that of WG increased by 168%. This could be attributed to the distinct thermal and combustion behaviours of the two materials, as well as the specific interactions between GO and each matrix. The dispersion and distribution of GO within the polymer matrix could also play a crucial role as it can impact how heat is conducted and how combustion products are generated, affecting the ignition behaviour differently. The increase in total heat release (THR) with the addition of GO shown in Table 6 reveals that the samples burnt for a long time due to the presence of a protective char layer restricting heat transfer to the sample.

The FPI (Fire Performance Index) and FIGRA (Fire Growth Rate Index) results provide valuable insights into the fire behaviour of the studied materials. The FPI values, which express the time to ignition relative to the heat release rate, indicate that the addition of graphene oxide (GO) generally influenced the materials' ignitability differently. The FPI values of neat PA11 and PA11_GO indicate no significant change in the fire performance, however, WG_GO exhibited a higher FPI, suggesting improved fire resistance with GO incorporation to WG. The FIGRA values, reflecting the rate of fire growth, highlighted the distinct effects of GO on combustion dynamics. Notably, neat PA11, PA11, and wheat gluten with GO exhibited lower FIGRA values, implying slower fire growth compared to neat WG.

Table 6: Reaction-to-fire properties of samples obtained from cone calorimeter tests.

Sample	PHRR (kW/m^2)	TTI (s)	THR (MJ/m^2)	FPI (m^2s/Kw)	FIGRA (kW/ms)
Neat PA11	1508.3 ± 122	182 ± 0	53.6 ± 6.2	0.12	8.3
PA11_GO	864.4 ± 114	88 ± 18	76.7 ± 2	0.1	9.8
Neat WG	652 ± 38	23 ± 4	13.1 ± 7.0	0.04	28.3
WG_GO	433 ± 40	61.7 ± 15	20.2 ± 10	0.14	7

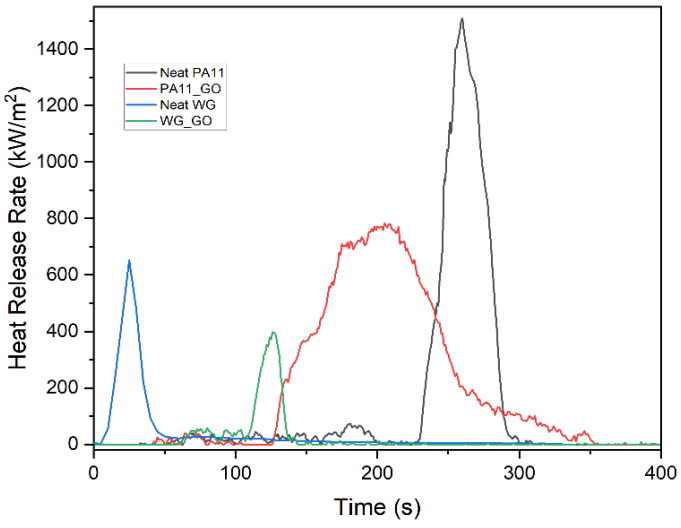

Fig. 5: Heat release rate curves of samples tested in the cone calorimeter.

3.3.2. Microscale Combustion Calorimeter Results

The addition of 2 wt% GO to PA11 slightly reduced the peak heat release rate (PHRR) by 4.6%, and peak temperature (PTemp) by 0.4%, but increased the heat release capacity (HRC) and total heat release (THR) values. This suggests that the addition of GO may have improved the flame retardancy of PA11, as the heat release rate during combustion decreased while the total heat release increased. The reduced PHRR and increased THR could indicate that GO likely created a protective char layer and reduced flammable gas concentration, making PA11 less flammable [66].

For WG, the addition of 2 wt% GO had little effect on the combustion properties. The PHRR, HRC, and THR values remained relatively unchanged, indicating that GO had a limited impact on the combustion behavior of WG. Comparing both plastics, the addition of 2 wt% GO appears to have a more significant effect on the combustion behavior of PA11 compared to WG. It led to a reduction in the peak heat release rate for PA11, which is a positive sign for its flammability, while not significantly affecting wheat gluten's combustion behavior, see Figure 6 and Table 7.

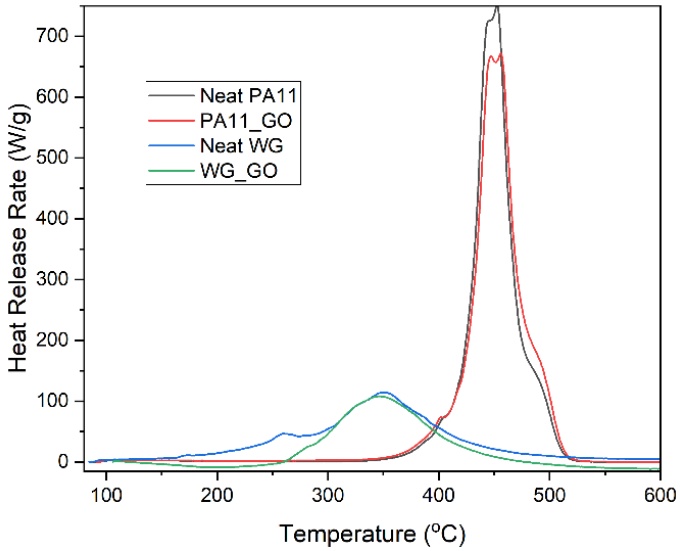

Fig. 6: Heat release rate curves of samples tested in the microscale combustion calorimeter.

Table 7: Heat release properties of samples tested with the MCC.

Sample	PHRR (W/g)	HRC (J/gK)	THR (kJ/g)	PTemp (°C)
Neat PA11	698.6 ± 38	730 ± 42	33.1 ± 0.4	445.5 ± 0.4
PA11_GO	666.6 ± 50	680 ± 48	33.8 ± 0.2	447.3 ± 6.1
Neat WG	113.8 ± 2	118 ± 0.7	14.3 ± 0	348.6 ± 1
WG_GO	113.5 ± 12	117 ± 15	11.8 ± 2	346.9 ± 1

3.3.3. Mechanical Properties

The provided data in Table 8 and Figure 7 demonstrates significant variations in the mechanical properties, including tensile strength, hardness, when 2 wt.% GO is introduced into both biobased WG and synthetic PA11 materials. Neat PA11, a synthetic polymer, exhibits substantially higher tensile strength at 42.5 MPa compared to neat WG, a biobased material, which has a much lower tensile strength of 5.4 MPa. Similarly, neat PA11 has the highest hardness at 74 MPa, indicating its resistance to deformation under a load [67]. On the other hand, neat WG has a lower hardness of 19 MPa, suggesting it is more deformable. However, the addition of GO to these materials (WG+GO and PA11+GO) leads to a considerable reduction in tensile strength, as evidenced by WG+GO's tensile strength of 2.05 MPa and PA11+GO's tensile strength of 15.02 MPa. While the reduction in tensile strength is influenced by factors like uneven GO dispersion and polymer matrix disruption, the impact on hardness may follow a similar trend, reflecting the complex interplay of material composition, dispersion quality, and interactions in designing advanced materials with tailored mechanical properties [67]. The mechanism behind this reduction in mechanical properties involves several factors. In the case of WG+GO, the likely uneven dispersion of GO within the biobased matrix results in weak interfacial bonding and stress concentration due to GO agglomeration. For PA11+GO, the presence of GO disrupts the polymer matrix, creating defects and interfering with the ability of the polymer to deform and stretch, ultimately leading to reduced tensile strength.

Table 8: Mechanical properties of neat and GO-added plastics.

Sample	Tensile strength (MPa)	Hardness (MPa)
Neat WG	5.4±0.2	19±2
WG+GO	2.05±0.02	14.75±0.5
Neat PA11	42.5±4.0	74±2
PA11+GO	15.02±0.6	40.05±0.4

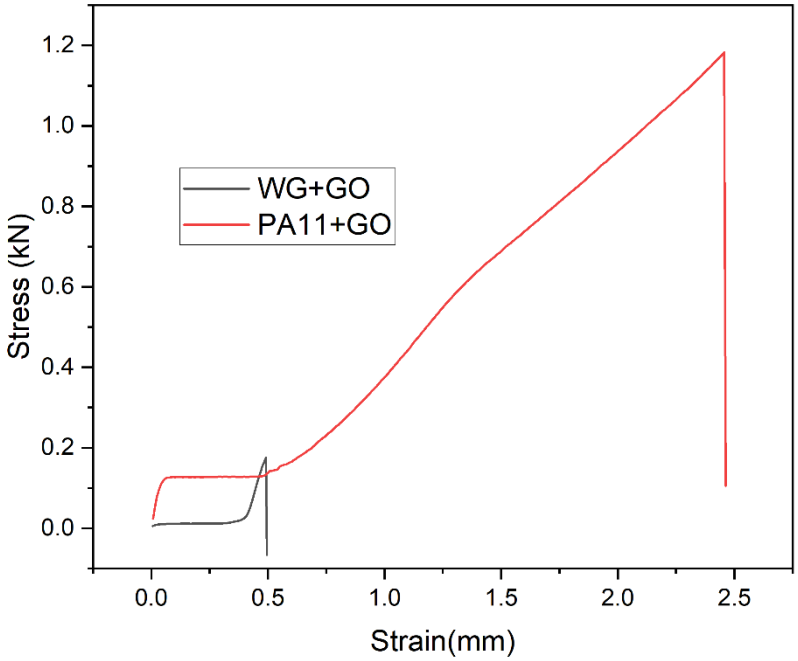

Fig. 7: Comparison of stress versus strain of the GO-added plastics

3.4. Integration of green chemistry principles and mechanisms involved in the facile preparation of graphene oxide from waste biomass

Green chemistry has a set of 12 principles aimed at designing and developing chemical processes and products that minimise or eliminate the use and generation of hazardous substances. By integrating these principles, green chemistry strives to promote environmental sustainability, protect human health, and foster the development of innovative and environmentally friendly solutions for a more sustainable future.[68] The current investigation satisfies six principles of green chemistry, namely, waste prevention, use of renewable resources, reduction of energy consumption, use of catalysts for efficiency, less hazardous synthesis, and reduction of derivatives. In the present study, a renewable resource (i.e., waste prevention and valorisation), in the form

of birch wood waste, was doped with manganese nitrate and pyrolysed at 950 °C to produce graphitic carbons without an intermediate amorphous carbon step, thus reducing the derivatives in the process. The doping of the wood particles with an effective catalyst (at low concentration) allowed the pyrolysis to take place at a lower temperature, 950 °C instead of temperatures greater than 1000 °C used in the conventional methods, which helped to promote energy efficiency. The entire synthesis was innocuous and no by-products, as derivates were formed.

Reports by several researchers show that metal nitrates are one of the best catalysts to produce graphitic carbon.[9,25,44] At temperatures above 250 °C during the graphitisation process, the metallic nitrates decompose into the corresponding metal oxides. The pyrolytic decomposition of cellulose, lignin, etc. present in the wood to amorphous carbon occurs at temperatures between 300 to 600 °C. The metal oxides are then reduced at temperatures above 600 °C to get converted into the corresponding metal nanoparticles. The final step is the transformation of the amorphous carbon in contact with the metallic nanoparticles into more ordered carbon structures at temperatures above 700 °C. The extent of graphitisation is dependent on the amount of amorphous carbon that comes into contact with the metallic nanoparticles.[69] The carbon that is far from the metal nanoparticles remains amorphous proving the necessity for efficient penetration and homogenous distribution of the catalyst into the biomass. This increases the effectiveness of the graphitisation process resulting in the production of graphitic carbon. In order to increase the penetration of the metal catalyst (manganese nitrate) into the pores of the birch wood and consequently enhance the effectiveness of the catalytic graphitisation, the wood was soaked under vacuum and subsequently heated in the current study. The generated graphite was washed with dilute HCL to dissolve the salts produced as a result of catalyst decomposition. Lastly, the graphite was milled with melamine to separate the graphitic layers into graphene. Since the milling process was not inert, the graphene was oxidised as shown in the TEM and EDX results. The entire process, doping, graphitisation, and milling are shown in Figure 8. The graphene

oxide produced from this study can be used in various applications including polymer composite manufacturing, flexible electronics, environmental remediation, etc.

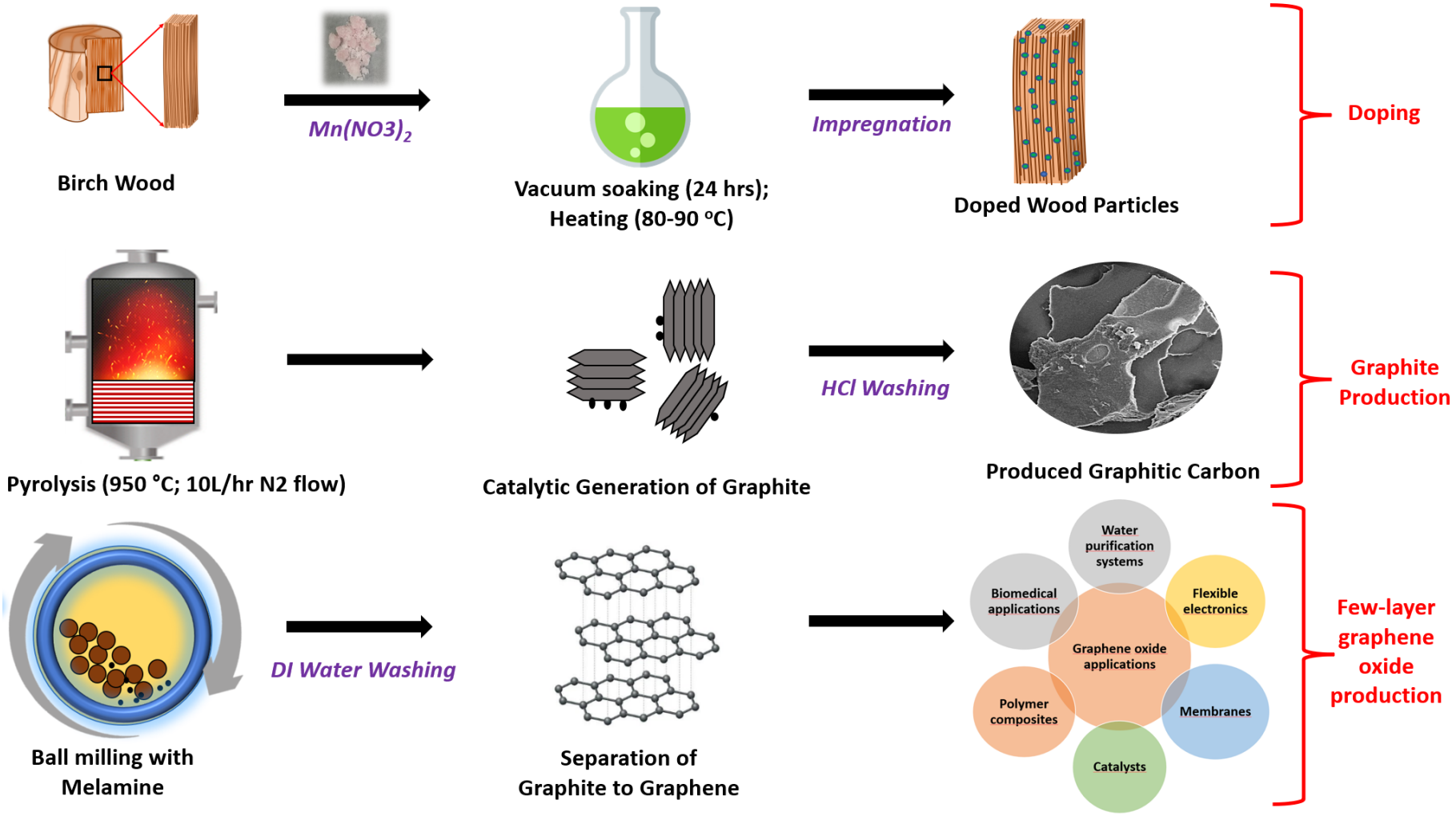

Fig. 8: A schematic diagram showing the direct conversion of birch wood to graphene oxide.

4. Conclusions

In this study, vacuum soaking, and heating at low temperatures (ca. 80 – 90 °C) were employed to efficiently dope a metal catalyst into the pores of wood followed by pyrolysis to develop graphitic carbon, which would be used subsequently to produce few-layer graphene oxide. This allows the direct conversion of sustainable biomass (here birch wood waste) into graphitic carbon without the intermediary step of producing amorphous carbon. The effect of four different concentrations of the catalyst and processing times were investigated. Graphite was successfully produced from manganese nitrate doped wood pyrolysed at 950 °C. Out of the four concentrations of catalysts (0.003, 0.005, 0.083, and 0.1 mol-metal/g) and two residence times (1 and 2 h), the sample with 0.005 mol-metal/g of catalyst heated for 2 h had the highest graphitisation degree (70%) from X-ray diffraction studies and the least defects from Raman spectroscopy. Hence, this sample was chosen and milled in a planetary ball mill with melamine as a dispersant and surfactant. The few-layer graphene oxide was characterised using UV-Vis, EDX, and TEM. The fluorescence in UV-Vis showed a broad peak at 230 nm, similar to graphene oxide dispersions, EDX showed the presence of oxygen in the sample and TEM revealed a semi-transparent structure with an irregular shape and variable layer thickness ranging from 3 to 8 analogous to that of graphene oxide. Based on the results, it can be concluded that few-layer graphene oxide has been successfully produced directly from waste wood without an intermediary amorphous carbon (biochar). Furthermore, to explore the applications of the produced graphene oxide, 2wt.% was added to polyamide 11 and wheat gluten plastics and subjected to a cone calorimeter test. The results showed a 42% and 33% reduction in peak heat release of the samples compared to the neat ones, which proved the effectiveness of the few-layer graphene oxide. In contrast, the microscale combustion calorimeter results showed minimal impact on the combustion behaviour of the plastics with the addition of GO. In terms of mechanical properties, the addition of GO resulted in a significant reduction in tensile strength for both materials, indicating a trade-off between enhanced flame resistance and reduced mechanical strength. The complex interplay of material composition and GO

dispersion highlights the need for a balanced approach when designing advanced materials with tailored properties.

Acknowledgments

The authors are thankful to Åforsk for generously funding the project (grant number: 21-179, project leader: Oisik Das).

References

1. Iqbal, S., Khatoon, H., Hussain Pandit, A. & Ahmad, S. Recent development of carbon based materials for energy storage devices. *Mater Sci Energy Technol* **2**, 417–428 (2019).
2. Jia, C., Dastafkan, K., Ren, W., Yang, W. & Zhao, C. Carbon-based catalysts for electrochemical CO 2 reduction. *Sustain Energy Fuels* **3**, 2890–2906 (2019).
3. Li, C. *et al.* Extreme nonlinear strong-field photoemission from carbon nanotubes. *Nat Commun* **10**, 4891 (2019).
4. Sevilla, M. & Fuertes, A. B. Graphitic carbon nanostructures from cellulose. *Chem Phys Lett* **490**, 63–68 (2010).
5. Bengtsson, A., Bengtsson, J., Sedin, M. & Sjöholm, E. Carbon Fibers from Lignin-Cellulose Precursors: Effect of Stabilization Conditions. *ACS Sustain Chem Eng* **7**, 8440–8448 (2019).
6. Plonska-Brzezinska, M. E. Carbon Nano-Onions: A Review of Recent Progress in Synthesis and Applications. *ChemNanoMat* **5**, 568–580 (2019).
7. Dhall, S. & Jaggi, N. Structural Studies of Functionalized Single-Walled Carbon Nano-Horns. *Fullerenes, Nanotubes and Carbon Nanostructures* **23**, 942–946 (2015).
8. Khosravi, F. *et al.* Development of a Highly Proliferated Bilayer Coating on 316L Stainless Steel Implants. *Polymers (Basel)* **12**, 1022 (2020).
9. Demir, M. *et al.* Graphitic Biocarbon from Metal-Catalyzed Hydrothermal Carbonization of Lignin. *Ind Eng Chem Res* **54**, 10731–10739 (2015).
10. Liu, W.-J., Jiang, H. & Yu, H.-Q. Development of Biochar-Based Functional Materials: Toward a Sustainable Platform Carbon Material. *Chem Rev* **115**, 12251–12285 (2015).
11. Pileidis, F. D. & Titirici, M.-M. Levulinic Acid Biorefineries: New Challenges for Efficient Utilization of Biomass. *ChemSusChem* **9**, 562–582 (2016).
12. Yang, H. *et al.* In-Depth Investigation of Biomass Pyrolysis Based on Three Major Components: Hemicellulose, Cellulose and Lignin. *Energy & Fuels* **20**, 388–393 (2006).
13. Paul T. Anastas & Warner, J. C. *Green chemistry : theory and practice*.
14. Behazin, E., Misra, M. & Mohanty, A. K. Compatibilization of toughened polypropylene/biocarbon biocomposites: A full factorial design optimization of mechanical properties. *Polym Test* **61**, 364–372 (2017).
15. Qian, K., Kumar, A., Zhang, H., Bellmer, D. & Huhnke, R. Recent advances in utilization of biochar. *Renewable and Sustainable Energy Reviews* **42**, 1055–1064 (2015).

16. Wissler, M. Graphite and carbon powders for electrochemical applications. *J Power Sources* **156**, 142–150 (2006).
17. MURADOV, N. & VEZIROGLU, T. "Green" path from fossil-based to hydrogen economy: An overview of carbon-neutral technologies. *Int J Hydrogen Energy* **33**, 6804–6839 (2008).
18. Dideikin, A. T. & Vul', A. Y. Graphene Oxide and Derivatives: The Place in Graphene Family. *Front Phys* **6**, (2019).
19. Wu, J., Lin, H., Moss, D. J., Loh, K. P. & Jia, B. Graphene oxide for photonics, electronics and optoelectronics. *Nat Rev Chem* **7**, 162–183 (2023).
20. Sontakke, A. D., Tiwari, S. & Purkait, M. K. A comprehensive review on graphene oxide-based nanocarriers: Synthesis, functionalization and biomedical applications. *FlatChem* **38**, 100484 (2023).
21. Smith, A. T., LaChance, A. M., Zeng, S., Liu, B. & Sun, L. Synthesis, properties, and applications of graphene oxide/reduced graphene oxide and their nanocomposites. *Nano Materials Science* **1**, 31–47 (2019).
22. Surovtseva, D., Crossin, E., Pell, R. & Stamford, L. Toward a life cycle inventory for graphite production. *J Ind Ecol* **26**, 964–979 (2022).
23. Zaira Zaman Chowdhury, Nurhidayatullaili Muhd Julkapli, Mohammed AbdulHakim Abdulrahma & Wageeh Yehye. Application of Graphitic Bio-Carbon using Two-Level Factorial Design for Microwave-assisted Carbonization. **11**, 3637–3659 (2016).
24. Sathish-Kumar, K., Vázquez-Huerta, G., Rodríguez-Castellanos, A., Poggi-Varaldo, H. M. & Solorza-Feria, O. Microwave assisted synthesis and characterizations of decorated activated carbon. *Int J Electrochem Sci* **7**, 5484–5494 (2012).
25. Major, I. *et al.* Graphitization of Miscanthus grass biocarbon enhanced by in situ generated FeCo nanoparticles. *Green Chemistry* **20**, 2269–2278 (2018).
26. Zaldivar, R. J. & Rellick, G. S. Some observations on stress graphitization in carbon-carbon composites. *Carbon N Y* **29**, 1155–1163 (1991).
27. Fu, T., Lv, J. & Li, Z. Effect of Carbon Porosity and Cobalt Particle Size on the Catalytic Performance of Carbon Supported Cobalt Fischer–Tropsch Catalysts. *Ind Eng Chem Res* **53**, 1342–1350 (2014).
28. Ōya, A. & Ōtani, S. Catalytic graphitization of carbons by various metals. *Carbon N Y* **17**, 131–137 (1979).
29. Marsh, H. & Latham, C. S. The Chemistry of Mesophase Formation. *ACS Symp Ser Am Chem Soc* (1983).
30. Logeswari, J., Pandurangan, A. & Sangeetha, D. An Efficient Catalyst for the Large Scale Production of Multi-Walled Carbon Nanotubes. *Ind Eng Chem Res* **50**, 13347–13354 (2011).
31. Lei, Z. *et al.* Nickel-Catalyzed Fabrication of SiO 2 , TiO 2 /Graphitized Carbon, and the Resultant Graphitized Carbon with Periodically Macroporous Structure. *Chemistry of Materials* **19**, 477–484 (2007).
32. Zhang, Y. *et al.* Recent advanced thermal interfacial materials: A review of conducting mechanisms and parameters of carbon materials. *Carbon N Y* **142**, 445–460 (2019).
33. Zhai, D., Du, H., Li, B., Zhu, Y. & Kang, F. Porous graphitic carbons prepared by combining chemical activation with catalytic graphitization. *Carbon N Y* **49**, 725–729 (2011).
34. McDonald-Wharry, J. S., Manley-Harris, M. & Pickering, K. L. Reviewing, Combining, and Updating the Models for the Nanostructure of Non-Graphitizing

Carbons Produced from Oxygen-Containing Precursors. *Energy & Fuels* **30**, 7811–7826 (2016).
35. Zickler, G. A., Smarsly, B., Gierlinger, N., Peterlik, H. & Paris, O. A reconsideration of the relationship between the crystallite size La of carbons determined by X-ray diffraction and Raman spectroscopy. *Carbon N Y* **44**, 3239–3246 (2006).
36. Jones, S. P., Fain, C. C. & Edie, D. D. Structural development in mesophase pitch based carbon fibers produced from naphthalene. *Carbon N Y* **35**, 1533–1543 (1997).
37. Maldonado-Hódar, F. J., Moreno-Castilla, C., Rivera-Utrilla, J., Hanzawa, Y. & Yamada, Y. Catalytic Graphitization of Carbon Aerogels by Transition Metals. *Langmuir* **16**, 4367–4373 (2000).
38. Deck, C. P. & Vecchio, K. Prediction of carbon nanotube growth success by the analysis of carbon–catalyst binary phase diagrams. *Carbon N Y* **44**, 267–275 (2006).
39. Rodriguez, N. M., Chambers, A. & Baker, R. T. K. Catalytic Engineering of Carbon Nanostructures. *Langmuir* **11**, 3862–3866 (1995).
40. Phounglamcheik, A., Wretborn, T. & Umeki, K. Increasing Efficiency of Charcoal Production with Bio-Oil Recycling. *Energy & Fuels* **32**, 9650–9658 (2018).
41. León, V. *et al.* Few-layer graphenes from ball-milling of graphite with melamine. *Chemical Communications* **47**, 10936 (2011).
42. Le, K. C., Henriksson, J. & Bengtsson, P. Polarization effects in Raman spectroscopy of light-absorbing carbon. *Journal of Raman Spectroscopy* **52**, 1115–1122 (2021).
43. Das, O., Sarmah, A. K. & Bhattacharyya, D. Structure–mechanics property relationship of waste derived biochars. *Science of The Total Environment* **538**, 611–620 (2015).
44. Vlahov, A. XRD graphitization degrees: a review of the published data and new calculations, correlations, and applications. *Geologica Balcanica* **50**, 11–35 (2021).
45. Gutiérrez-Pardo, A., Ramírez-Rico, J., de Arellano-López, A. R. & Martínez-Fernández, J. Characterization of porous graphitic monoliths from pyrolyzed wood. *J Mater Sci* **49**, 7688–7696 (2014).
46. Ferrari, A. C. & Robertson, J. Interpretation of Raman spectra of disordered and amorphous carbon. *Phys Rev B* **61**, 14095–14107 (2000).
47. Ferrari, A. C. & Basko, D. M. Raman spectroscopy as a versatile tool for studying the properties of graphene. *Nat Nanotechnol* **8**, 235–246 (2013).
48. Sadezky, A., Muckenhuber, H., Grothe, H., Niessner, R. & Pöschl, U. Raman microspectroscopy of soot and related carbonaceous materials: Spectral analysis and structural information. *Carbon N Y* **43**, 1731–1742 (2005).
49. Petrov, D. V., Matrosov, I. I., Sedinkin, D. O. & Zaripov, A. R. Raman Spectra of Nitrogen, Carbon Dioxide, and Hydrogen in a Methane Environment. *Opt Spectrosc* **124**, 8–12 (2018).
50. Wall, M. *The Raman Spectroscopy of Graphene and the Determination of Layer Thickness*. (2011).
51. Tuinstra, F. & Koenig, J. L. Characterization of Graphite Fiber Surfaces with Raman Spectroscopy. *J Compos Mater* **4**, 492–499 (1970).
52. McDonald-Wharry, J., Manley-Harris, M. & Pickering, K. Carbonisation of biomass-derived chars and the thermal reduction of a graphene oxide sample

studied using Raman spectroscopy. *Carbon N Y* **59**, 383–405 (2013).
53. Richter, A., Ries, R., Smith, R., Henkel, M. & Wolf, B. Nanoindentation of diamond, graphite and fullerene films. *Diam Relat Mater* **9**, 170–184 (2000).
54. Paris, O., Zollfrank, C. & Zickler, G. A. Decomposition and carbonisation of wood biopolymers—a microstructural study of softwood pyrolysis. *Carbon N Y* **43**, 53–66 (2005).
55. Das, O., Sarmah, A. K. & Bhattacharyya, D. Nanoindentation assisted analysis of biochar added biocomposites. *Compos B Eng* **91**, 219–227 (2016).
56. Zickler, G. A., Schöberl, T. & Paris, O. Mechanical properties of pyrolysed wood: a nanoindentation study. *Philosophical Magazine* **86**, 1373–1386 (2006).
57. Lai, Q., Zhu, S., Luo, X., Zou, M. & Huang, S. Ultraviolet-visible spectroscopy of graphene oxides. *AIP Adv* **2**, (2012).
58. Puangbuppha, B., Limsuwan, P. & Asanithi, P. Non-Chemically Functionalized Graphene Exfoliated from Graphite in Water using Ultrasonic Treatment. *Procedia Eng* **32**, 1094–1099 (2012).
59. Li, F., Li, L., Wang, W. & Gao, J. A new facile approach to prepare reduced graphene oxide and MoO2/reduced graphene oxide as electrode materials for oxygen reduction reactions. *J Colloid Interface Sci* **519**, 194–202 (2018).
60. Zhang, T. *et al.* The UV absorption of graphene oxide is size-dependent: possible calibration pitfalls. *Microchimica Acta* **186**, 207 (2019).
61. Mahmoud, A. E. D., Stolle, A. & Stelter, M. Sustainable Synthesis of High-Surface-Area Graphite Oxide via Dry Ball Milling. *ACS Sustain Chem Eng* **6**, 6358–6369 (2018).
62. Chang, Y.-S., Chen, F.-K., Tsai, D.-C., Kuo, B.-H. & Shieu, F.-S. N-doped reduced graphene oxide for room-temperature NO gas sensors. *Sci Rep* **11**, 20719 (2021).
63. Ma, J., Yang, M., Yu, F. & Zheng, J. Water-enhanced Removal of Ciprofloxacin from Water by Porous Graphene Hydrogel. *Sci Rep* **5**, 13578 (2015).
64. Aziz, M., Abdul Halim, F. S. & Jaafar, J. Preparation and Characterization of Graphene Membrane Electrode Assembly. *J Teknol* **69**, (2014).
65. Jin, X. *et al.* The synergism between melamine and expandable graphite on improving the flame retardancy of polyamide 11. *High Perform Polym* **29**, 77–86 (2017).
66. Haewon Kim. Effects of Several Phosphorus-based Flame-Retardant Additives to the Thermal and Flammability Properties of PA6/66, PA11, and PA12 Polymers . in (2018).
67. Bahrami, M., Abenojar, J. & Martínez, M. A. Comparative Characterization of Hot-Pressed Polyamide 11 and 12: Mechanical, Thermal and Durability Properties. *Polymers (Basel)* **13**, 3553 (2021).
68. Anastas, P. T. & John C. Warner. Principles of green chemistry. *Green chemistry: Theory and practice* **29**, 14821–42 (1998).
69. Sevilla, M., Sanchís, C., Valdés-Solís, T., Morallón, E. & Fuertes, A. B. Direct synthesis of graphitic carbon nanostructures from saccharides and their use as electrocatalytic supports. *Carbon N Y* **46**, 931–939 (2008).